

# Hierarchical Multi-Resolution Graph-Cuts for Water-Fat-Silicone Separation in Breast MRI

Jonathan K. Stelter<sup>1</sup>, Christof Boehm<sup>1</sup>, Stefan Ruschke<sup>1</sup>, Kilian Weiss<sup>1</sup>, Maximilian N. Diefenbach, Mingming Wu, Tabea Borde, Georg P. Schmidt, Marcus R. Makowski, Eva M. Fallenbergl, and Dimitrios C. Karampinos<sup>1</sup>

**Abstract**—Water-fat separation is a non-linear non-convex parameter estimation problem in magnetic resonance imaging typically solved using spatial constraints. However, there is still limited knowledge on how to separate in vivo three chemical species in the presence of magnetic field inhomogeneities. The proposed method uses multiple graph-cuts in a hierarchical multi-resolution framework to perform robust chemical species separation in the breast for subjects with and without silicone implants. Experimental results show that the proposed method can decrease the computational time for water-fat separation and perform accurate water-fat-silicone separation with only a limited number of acquired echo images at 3T. The silicone-separated images have an improved spatial resolution and image contrast compared to conventional scans used for regular monitoring of the silicone implant's integrity.

**Index Terms**—Chemical shift encoding-based water-fat separation, dixon imaging, breast magnetic resonance imaging, hierarchical decomposition, silicone implants.

## I. INTRODUCTION

SILICONE implants are commonly used for breast augmentation or breast reconstruction after mastectomy. However, aging implants weaken and there is the risk

Manuscript received 15 April 2022; revised 24 May 2022; accepted 30 May 2022. Date of publication 3 June 2022; date of current version 27 October 2022. This work was supported in part by the European Research Council [Magnetic resonance imaging platform for probing fat microstructure (ProFatMRI)] under Grant 677661 and in part by the Philips Healthcare. (Corresponding author: Jonathan K. Stelter.)

This work involved human subjects or animals in its research. Approval of all ethical and experimental procedures and protocols was granted by the Ethics Committee of the Klinikum rechts der Isar, Technical University of Munich, Munich, Germany under Application No. 21/61 S-KK.

Jonathan K. Stelter, Christof Boehm, Stefan Ruschke, Maximilian N. Diefenbach, Mingming Wu, Tabea Borde, Marcus R. Makowski, Eva M. Fallenbergl, and Dimitrios C. Karampinos are with the Department of Diagnostic and Interventional Radiology, Klinikum rechts der Isar, Technical University of Munich, 81675 Munich, Germany (e-mail: jonathan.stelter@tum.de; christof.boehm@tum.de; stefan.ruschke@tum.de; maxdiefenbach@protonmail.com; mingming.wu@tum.de; tabea.borde@tum.de; marcus.makowski@tum.de; eva.fallenbergl@tum.de; dimitrios.karampinos@tum.de).

Kilian Weiss is with Philips Healthcare, 22335 Hamburg, Germany (e-mail: kilian.weiss@philips.com).

Georg P. Schmidt is with the Department of Gynecology and Obstetrics, Klinikum rechts der Isar, Technical University of Munich, 81675 Munich, Germany, and also with the Comprehensive Cancer Center (CCCTUM), Technical University of Munich, 81675 Munich, Germany (e-mail: georgphilipp.schmidt@mri.tum.de).

Digital Object Identifier 10.1109/TMI.2022.3180302

for ruptures leading to inflammation or silicone granuloma formation [1]. Magnetic Resonance Imaging (MRI) is a sensitive method for monitoring the implant's integrity [1]. Clinically, T2-weighted turbo spin echo acquisitions using double inversion recovery (DIR) for water and fat suppression or combining frequency-selective water suppression and short tau inversion recovery (STIR) for fat suppression are used to generate silicone-only images with bright silicone signal [2], [3]. However, the acquired silicone-only images typically suffer from low signal-to-noise ratio (SNR), coarse interslice resolution, motion sensitivity and long scan times. For example, the conventional silicone-only sequence in our institution applies an acquisition voxel size of 3 mm in the slice selection direction, whereas an isotropic scan of higher resolution would enable the assessment of the silicone's integrity for different image orientations and reduce partial volume effects.

Chemical shift encoding-based water-fat separation (CSE-WFS) has been previously combined with STIR to perform water-silicone separation in fat suppressed T2-weighted turbo spin-echo imaging [4]. CSE-WFS has been also recently combined with multi-echo gradient echo imaging to measure the fat fraction and magnetic susceptibility properties in the breast. Thus, CSE-WFS enables the quantification of breast density [5] using the proton density fat-fraction (PDFF) [6], [7], as high breast density has been identified as a risk factor for breast cancer [8]. The water-fat separation problem is a separable non-linear non-convex least-squares optimization problem and can be reformulated as a field-map estimation problem. Often, separation relies on a spatial smoothness constraint due to sensitivity to noise and the ambiguity of the model when only a single species is present. Previous algorithms to solve the water-fat separation problem include region growing schemes [9], [10], multi-resolution optimization [11]–[14], graph search [15]–[18] or also neural networks [19].

On the one hand, graph search-based algorithms have been particularly effective in solving the water-fat separation problem in the presence of large field-map variations. The first introduced graph search-based formulation of the water-fat separation problem iteratively evaluated two field-map candidates per voxel based on a cost function [15]. Upon convergence to a specified criterion, the field-map solution was optimal to an exponentially large set [15] but did not

necessarily converge to the global minimum. Single-min-cut graph-cut algorithms were introduced with global convergence, non-smoothed field-maps and inter-slice regularization [16]–[18]. The rapid globally optimal surface estimation algorithm [17] and the variable-layer single-min-cut graph-cut algorithm (vLGC) [18] restricted the solution voxel-wise to its set of local minima. The vLGC algorithm allowed furthermore for a varying number of minima per voxels and was able to resolve large field-map variations [18]. However, graph-cut algorithms still often suffer from long processing times and, thus, may be difficult to incorporate into standard clinical workflows.

On the other hand, multi-resolution algorithms solve the field-mapping problem using different image resolutions by starting from coarse graining and concluding with fine details. Multi-resolution algorithms rely on the assumption of a slowly varying field-map aiming for an increased robustness in the presence of noise. The first presented approach used a golden section search at the coarsest resolution and refined the field-map for increasingly finer resolutions [11]. In this method, field-mapping was susceptible to water-fat swaps if the initialization was wrong (i.e. shifted center frequency). Another multi-resolution optimization algorithm used direct phase estimation to avoid field-map wrapping [12]. The method could handle arbitrary species showing separation results for a single slice of a water–oil–silicone phantom. However, the method was not able to estimate an unwrapped field-map which can be of high importance for subsequent processing steps, such as quantitative susceptibility mapping [20]. In [13], the presented algorithm combined the multi-resolution approach with graph-cuts. The single quadratic pseudo-Boolean optimization (QPBO) graph-cut algorithm was applied in each layer of the multi-scale framework. Field-map solutions were propagated from coarse to finer scales if voxels were not resolved by the graph-cut. Results showed promising improvements for noise-dominated regions, although accuracy was only slightly improved compared to the single-resolution graph-cut in [16]. Field-map unwrapping needed to be performed separately. Another study also showed the advantage of incorporating spatial smoothing in the QPBO algorithm [14].

Despite the availability of the above algorithms, there is still limited knowledge on how to simultaneously separate three chemical species in the presence of water, fat, and silicone in in vivo breast imaging. Incorporating silicone to the signal model increases the complexity of the chemical species separation problem. Water-fat-silicone separation was already performed in a phantom [12], [21], but both approaches were not applied in vivo and are limited due to the needed field map initialization or direct phase estimation. Initial results on in vivo water-fat-silicone separation applied a modified single-resolution vLGC algorithm showing successful separation for 6 echoes but significantly reduced noise performance for fewer echoes leading to water-fat-silicone swaps [22].

The present work aims to develop a methodology for the joint estimation of water, fat and silicone images and the field-map. A hierarchical decomposition of the problem

combined with a multi-resolution formulation of the vLGC algorithm is developed for faster processing times. At the same time, we aim at comparable field-map accuracy in subjects without silicone implants and a high robustness, also with limited acquired echoes, for in vivo separation for subjects with silicone implants. Phantom and in vivo MR measurements are performed to compare the developed method with the vLGC algorithm and to evaluate its ability to overcome limitations of the conventional silicone-only scan.

## II. THEORY

CSE-WFS encodes the difference in resonance frequency for the different chemical species by acquiring several echo images at different echo times. Gradient echo [21], [23]–[25], spin echo [26] and fast spin echo [4], [27] sequences have been proposed for water-fat imaging and might be extended for an additional third chemical species.

### A. Signal Model

In water-fat imaging, the complex voxel signal  $s_{WF}(t_n)$  at an echo time  $t_n$  can be modeled taking into consideration  $T_2^*$  decay effects [23], [28] and a multi-peak model for the fat spectrum [28]. Here, an equal transverse relaxation rate  $R_2^*$  is assumed for all peaks [28].

$$s_{WF}(t_n) = (\rho_W + \rho_F c_n) e^{\gamma t_n}, \quad \gamma = i2\pi f_B - R_2^* \quad (1)$$

with  $\rho_W$ ,  $\rho_F$  the complex species signals of water and fat and  $\gamma = i2\pi f_B - R_2^*$  a coefficient describing the  $T_2^*$ -decay and the local frequency shift due to the static field inhomogeneity  $f_B$ . For the fat spectrum  $c_n$ ,  $P$  is the total number of spectral peaks,  $\alpha_p$  the relative amplitude and  $f_{F,p}$  the resonance frequency relative to water for the  $p$ -th fat peak:

$$c_n = \sum_{p=1}^P \alpha_p e^{i2\pi f_{F,p} t_n} \quad \text{with} \quad \sum_{p=1}^P \alpha_p = 1 \quad (2)$$

In water-fat-silicone imaging, the signal model needs to be extended to include the complex silicone signal  $\rho_S$ . The silicone component can be specified as a single peak with relative resonance frequency  $f_S$ . Previous studies have shown a chemical shift of approximately -4.9 ppm for the silicone relative to water at body temperature [29].

$$s_{WFS}(t_n) = s_{WF}(t_n) + \rho_S e^{i2\pi f_S t_n} e^{\gamma t_n} \quad (3)$$

The signal model can then be rewritten using the matrix representation:

$$\underbrace{\begin{pmatrix} s(t_1) \\ \vdots \\ s(t_N) \end{pmatrix}}_s = \underbrace{\begin{pmatrix} e^{\gamma t_1} & c_1 e^{\gamma t_1} & e^{(\gamma + i2\pi f_S)t_1} \\ \vdots & \vdots & \vdots \\ e^{\gamma t_N} & c_N e^{\gamma t_N} & e^{(\gamma + i2\pi f_S)t_N} \end{pmatrix}}_{\Psi(\gamma)} \underbrace{\begin{pmatrix} \rho_W \\ \rho_F \\ \rho_S \end{pmatrix}}_{\rho} \quad (4)$$

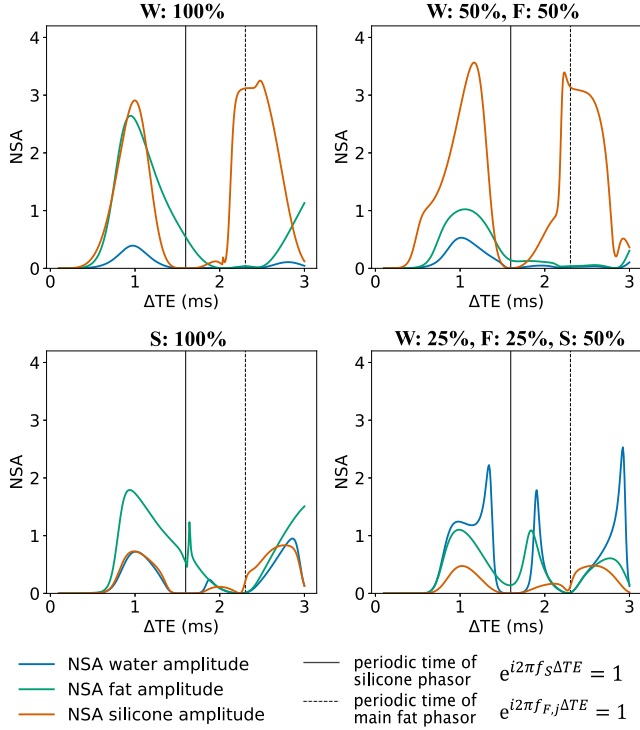


**Fig. 1.** Noise performance for water-fat-silicone separation depending on the echo spacing  $\Delta TE$  at 3T with constant  $TE_1 = 1.58$  ms,  $R_2^* = 40$  Hz,  $f_B = 0$  Hz. An exact knowledge of the field-map was assumed. The number of signal averages (NSA) for the water (W), fat (F) and silicone (S) signal amplitude is shown for different water-fat-silicone fractions and 4 echoes.

## B. Noise Performance

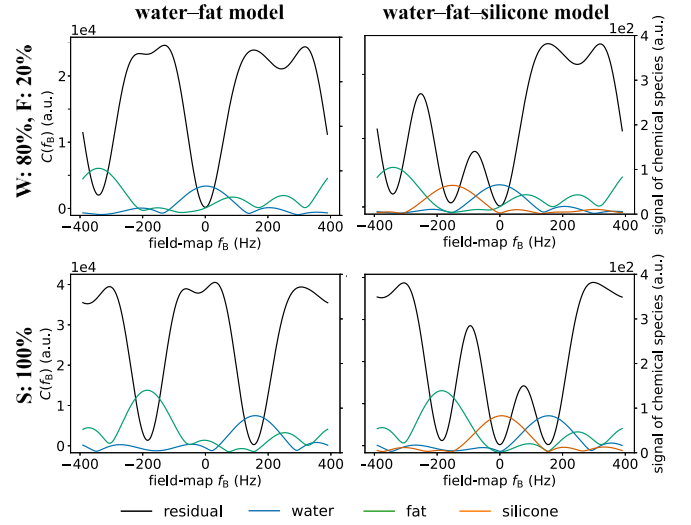
The noise properties of the separated images are dependent on the assumed signal model and can be optimized by the choice of echo times. A theoretical limit can be estimated by the minimal noise variance using the Fisher Information Matrix in the Cramér-Rao lower bound (CRLB) analysis [30], [31]. The noise variance can be expressed by the number of signal averages (NSA) [30], [31].

Figure 1 summarizes the noise performance depending on the echo spacing  $\Delta TE$  for water-fat-silicone separation with 4 echoes at 3T. The noise performance is optimal for an echo spacing of about 1 ms. Higher echo spacings show additional maxima for some parameters but not simultaneously for water, fat and silicone. A worse performance is reported for  $\Delta TE \approx 1.6$  ms corresponding to the echo times when the silicone phasor is similar in all acquired echoes ( $e^{i2\pi f_S \Delta TE} = 1$ ).

## C. Parameter Estimation

Complex-based and magnitude-based parameter estimation techniques have been presented for water-fat separation. Complex-based parameter estimation needs to correct for several phase errors, especially for bipolar gradient echo acquisitions [25] but has demonstrated a superior noise performance and fat modelling accuracy compared to magnitude-based techniques [32].

The present work is based on a complex-based parameter estimation technique using magnitude and phase images. Four



**Fig. 2.** Residual  $C(f_B)$  (black line) for the water-fat (left) and water-fat-silicone (right) signal model and 6 echoes at 3T. The model predicted water (blue), fat (green) and silicone (orange) signals are depicted using colored lines. Two voxels with different simulated chemical composition (W: water, F: fat, S: silicone), fat fraction of 20% and no silicone (top) or pure silicone (bottom), true field-map of 0 Hz,  $R_2^* = 40$  Hz and Rician noise (SNR = 100) are shown. The residuals are shown for one period length  $f_{B,period}$  of the field-map.

echoes are the minimum required echo images to solve Eq. 3 with its seven free parameters if  $T_2^*$  decay is neglected.

The mean-square error  $\mathcal{C}(\gamma)$  between model and measured data is minimized voxel-wise for parameter estimation. First, it is solved for the field-map using variable projection (VARPRO) [33]:

$$\mathcal{C}(\gamma) = \|\mathbf{s} - \Psi(\gamma)\boldsymbol{\rho}\|_2^2 = \|\mathbf{I} - \Psi(\gamma)\Psi^\dagger(\gamma)\mathbf{s}\|_2^2 \quad (5)$$

Water, fat and silicone signals can be computed based on the field-map:

$$\begin{aligned} \hat{f}_B &= \underset{f_B}{\operatorname{argmin}} \mathcal{C}(f_B) = \underset{f_B}{\operatorname{argmin}} \mathcal{C}(\gamma = i2\pi f_B) \\ \hat{\boldsymbol{\rho}} &= \Psi^\dagger(\gamma = i2\pi \hat{f}_B)\mathbf{s} \end{aligned} \quad (6)$$

$R_2^*$  can be neglected for field-map estimation due to uncorrelated estimates but needs to be considered for PDF estimation:

$$\hat{R}_2^* = \underset{R_2^*}{\operatorname{argmin}} \mathcal{C}(R_2^*) = \underset{R_2^*}{\operatorname{argmin}} \mathcal{C}(\gamma = i2\pi \hat{f}_B - R_2^*) \quad (7)$$

The residual  $\mathcal{C}(f_B)$  is compared in Fig. 2 for two different water-fat-silicone fractions and for the water-fat and water-fat-silicone signal models. In the case of constant echo spacings, the residual as a function of  $f_B$  is periodic with period  $f_{B,period} = \frac{1}{\Delta TE}$ . The water-fat-swapped solution has a higher residual error due to the multi-peak modelling of fat and, therefore, mitigates the ambiguity of the chemical species separation for a fat-containing voxel.  $\mathcal{C}(f_B)$  shows an additional minimum corresponding to the silicone solution if the water-fat-silicone model is assumed. The minima are well separated in Fig. 2 for 6 echoes, but the minima are strongly broadened for only 4 acquired echoes (Fig. 3). In such a case of

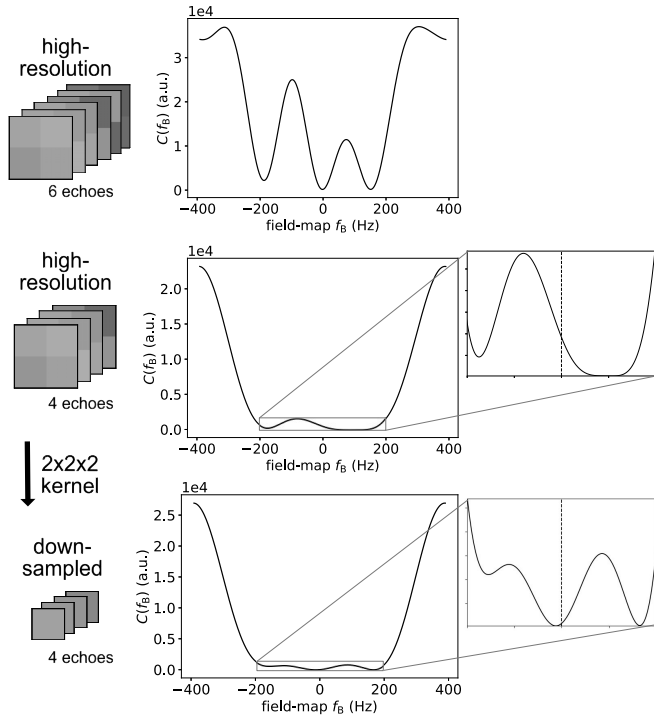


Fig. 3. Residual  $C(f_B)$  for 4 and 6 echoes and low SNR ( $\text{SNR} = 10$ ). A simulated voxel with only silicone, true field-map of 0 Hz and  $R_2^* = 40$  Hz is shown. At the top, the minima are distinctive for 6 echoes. In the center, 4 echoes were used for simulation leading to a plateau with no minima at 0 Hz. At the bottom, the voxel was averaged with neighboring voxels using a  $2 \times 2 \times 2$  kernel leading to a better noise performance. The residuals are shown for one period length  $f_{B,\text{period}}$  of the field-map.

broadened minima, the SNR needs to be increased for reliable field-map estimation, e.g. averaging of neighboring voxels.

### III. PROPOSED METHOD

A method is developed using hierarchical decomposition to solve the separation problem based on multiple graph-cut layers. Each graph-cut layer has a specific function and the information of previous layers is incorporated by inserting these field-maps as priors for subsequent graph-cut processing (Fig. 4).

#### A. Single Layer: Graph-Cut Algorithm for Field-Mapping

The single graph-cut layer is based on the vIGC algorithm for water-fat separation [18]. A penalized maximum likelihood cost function is used as a smoothness constraint and the minimization problem is transformed to a surface estimation problem using the graph-cut algorithm proposed in [34]: An energy function  $E(S)$  is minimized by computing a maximum flow of a graph with  $S(\mathbf{r})$  a local minima of the mean-square error  $\mathcal{C}(\mathbf{r}, f_B)$ :

$$S(\mathbf{r}) \in B_{\mathbf{r}} = \{x \in A \mid x = \underset{y \in U^o, U \subset A}{\operatorname{argmin}} C(\mathbf{r}, y)\} \\ \text{for } \mathbf{r} \in M = \{(x, y, z) \mid \text{MIP}_{\text{TE}}(x, y, z) > T * \text{MIP}_{\text{TE},\text{max}}\} \quad (8)$$

with  $B_{\mathbf{r}}$  the set of graph nodes for the voxel  $\mathbf{r}$  given by the local minima of  $\mathcal{C}(\mathbf{r}, f_B)$  in the sampling range,  $A$  the set of

sampling points,  $U^o$  the interior of a neighborhood  $U$  and  $M$  the mask to distinguish between signal and no-signal regions.  $\text{MIP}_{\text{TE}}$  is the maximum signal intensity projection over echo times,  $\text{MIP}_{\text{TE},\text{max}}$  its maximum value and  $T$  is a threshold.

The Boykov-Kolmogorov algorithm [35] is applied for max-flow computation and the field-map is reconstructed based on the partition of the minimum cut [18], [34].

In this work, several parameters are defined for the graph-cut algorithm which can be adapted for different layers:

1) *Spatial Resolution*: The graph-cut can be performed on a downsampled signal since the field-map is slowly varying. The 3D-image array is first scaled to match the aimed voxel size (Section III-B) in slice and in-plane direction using second-order spline interpolation. The residual  $\mathcal{C}(\mathbf{r}, f_B)$  is then computed at the reduced spatial resolution. After graph-cut solving, the resulting field-map can be low-pass filtered using a Gaussian kernel ( $\sigma = \alpha_\sigma$  with  $\alpha_\sigma = 1$  an empirically chosen value) and is reversely scaled for the original spatial resolution based on the reconstruction voxel size.

Interpolation is hampered in masked regions due to missing information outside of the mask. Image inpainting is thus applied slice-wise to fill missing phase and field-map information for interpolation near to the mask boundary using the algorithm in [36]. The algorithm uses a fast marching method [37] to propagate the information from the unmasked image regions along the image gradient by computing a weighted average of the known image values.

2) *Energy Function and Regularization Parameter*: The energy function is extended for an additional data cost term given by the residual  $\mathcal{C}(\mathbf{r}, f_B)$  compared to the vIGC algorithm [18]:

$$E(S) = \underbrace{\frac{1}{\lambda} \sum_{\mathbf{r}} d(\text{MIP}_{\text{TE}}) * d_{\mathbf{r}}(\mathcal{C}(\mathbf{r}, S(\mathbf{r})))}_{\text{data cost term}} + \underbrace{\sum_{\mathbf{r}} \sum_{s \in N(\mathbf{r})} |S(\mathbf{r}) - S(s)|^2}_{\text{smoothness term}} \quad (9)$$

with  $N(\mathbf{r})$  the voxel neighborhood defined by directly adjacent voxels.  $d, d_{\mathbf{r}}$  are a global and a voxel-wise mapping to the interval  $[0, 1]$ , respectively. The regularization parameter  $\lambda$  determines the compromise between spatial smoothness and data consistency and is optimized to minimize water-fat-silicone swaps in the validation dataset.

Intra-edges between graph nodes are calculated using the data cost term and inter-edges are calculated using the smoothness term [34].

3) *Signal Model*: The residual  $\mathcal{C}(\mathbf{r}, f_B)$  can be computed for different assumed signal models (e.g. Eqs. 1 and 3). A lower regularization ( $\lambda = 10^{-4}$ ) is used for the water-fat-silicone model to account for the increased number of minima with different depths compared to the water-fat model.

4) *Field-Map Priors*: The field-map solution of previous graph-cut layers can be used as an initialization for the graph-cut algorithm. In detail, the sampling range per voxel  $A_{\mathbf{r}}$  can be chosen in the neighborhood  $[f_0, f_1]$  of the field-map

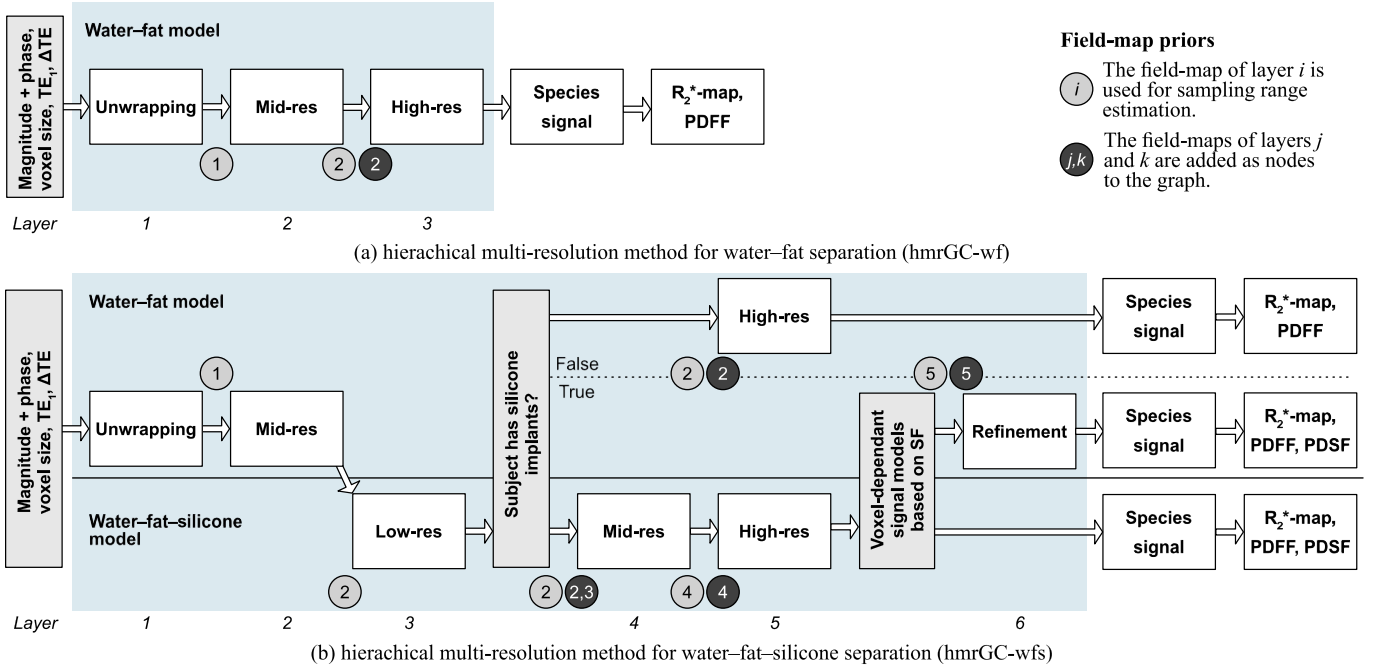


**Fig. 4.** Schematic diagram for two hierarchical multi-resolution methods: (a) hierarchical multi-resolution method for water-fat separation (hmrGC-wf), (b) hierarchical multi-resolution method for water-fat-silicone separation (hmrGC-wfs). Both methods consist of layered graph-cuts for field-mapping (blue area) and layers for species signal,  $R_2^*$ , proton density fat-fraction (PDFF) and proton density silicone-fraction (PDSF) estimation. The graph-cut layers used as field-map priors for sampling range estimation and graph nodes insertion are denoted.

prior  $f_{\text{prior}}(\mathbf{r})$ :

$$A_r = \{x \in [f_{\text{prior}}(\mathbf{r}) - f_0, f_{\text{prior}}(\mathbf{r}) + f_1] \mid x = f_{\text{prior}}(\mathbf{r}) - f_0 + k * \Delta f, k \in \mathbb{N}\} \quad (10)$$

with  $\Delta f$  the sampling stepsize. Alternatively, the prior can be added as nodes to the graph. The set of local minima  $B_r$  is therefore extended for the set containing the field-map prior if there is no local minimum in a specified neighborhood  $[f'_0, f'_1]$ :

$$B'_r = B_r \cup \{f_{\text{prior}}(\mathbf{r}) \mid B_r \cap [f_{\text{prior}}(\mathbf{r}) - f'_0, f_{\text{prior}}(\mathbf{r}) + f'_1] = \emptyset\} \quad (11)$$

## B. Multiple Layers: Hierarchical Multi-Resolution Graph-Cuts

**1) Water-Fat Separation (hmrGC-Wf):** A three layer multi-resolution graph-cut method is defined with a single signal model for water-fat separation (Fig. 4 a): First, water-fat separation is performed for a downsampled signal (voxel size: 5.5 mm) and a large sampling range (e.g.  $2.5 * f_{B,\text{period}}$ ). The regularization is reduced ( $\lambda = 10^{-4}$ ) due to higher SNR in the low-resolution signal. The resulting low-resolution field-map is used as an unwrapped initialization for the next layer. Two subsequent layers are performed with medium (*Mid-res*, voxel size: 1.5 mm) and high resolution (*High-res*, reconstructed voxel size). If the reconstructed voxel size is equal or larger than 1.5 mm in the slice direction and the in-plane directions, the medium resolution layer is skipped. Additionally, the solution of the *Mid-res* layer is directly inserted as graph nodes to the *High-res* layer to account for voxels dominated by noise.

**2) Water-Fat-Silicone Separation (hmrGC-Wfs):** The proposed method for breast MRI performs water-fat or water-fat-silicone separation based on the presence of silicone implants. Hyperparameters for the several graph-cut layers are summarized in Table I.

First, unwrapping and a medium resolution field-map calculation is performed similarly to hmrGC-wf. A water-fat signal model is assumed, although silicone implants may be present. Thus, in a subsequent *Low-res* (WFS) and *Mid-res* (WFS) layer, a sampling neighborhood  $[f_0, f_1]$  is chosen based on the water-fat prior allowing swapping from fat to silicone:

$$[f_0, f_1] = [-\zeta, \zeta + \Delta_{\text{WF}}] \quad (12)$$

with  $\zeta = \alpha_\zeta f_{\text{center}}$  a margin,  $\alpha_\zeta = 0.4 * 10^{-6}$  an empiric hyperparameter,  $f_{\text{center}}$  the center frequency and  $\Delta_{\text{WF}} = f'_{B,\text{water}} - f_{B,\text{fat}}$  the field-map frequency distance between the fat  $f_{B,\text{fat}}$  and the upward water solution  $f'_{B,\text{water}} = f_{B,\text{water}} + f_{B,\text{period}}$ . The silicone peak is within this distance.

After the *Low-res* (WFS) layer, the proton density silicone-fraction (PDSF) is calculated. Calculation is performed similarly to the PDFF with correction for noise bias effects using a magnitude discrimination approach [6], [38] based on a generalized proton density fraction  $\eta_i$  with  $i \in \{W, F, S\}$  the different chemical species:

$$\eta_i = \begin{cases} \frac{|\rho_i|}{|\sum_j \rho_j|} & \text{if } \frac{|\rho_i|}{|\sum_j \rho_j|} > 0.5 \\ 1 - \frac{|\sum_{j \neq i} \rho_j|}{|\sum_j \rho_j|} & \text{otherwise} \end{cases} \quad (13)$$

$$\text{PDSF} = \eta_S \quad (14)$$

TABLE I

GRAPH-CUT PARAMETERS FOR THE HIERARCHICAL MULTI-RESOLUTION METHOD FOR WATER-FAT-(SILICONE) SEPARATION (HMRGC-WFS). THE SAMPLING AND INSERTION NEIGHBORHOODS ARE GIVEN IN PPM ( $f_B[\text{PPM}] = f_B[\text{Hz}]/f_{\text{CENTER}}[\text{Hz}] * 10^6$ ) WITH  $f_{\text{CENTER}}$  THE CENTER FREQUENCY

layer	property	value
1 Un-wrapping	voxel size	5.5 mm
	signal model	water-fat
	regularization parameter $\lambda$	$10^{-4}$
	field-map low-pass filter	Gaussian ( $\sigma = 1$ )
2 Mid-res (WF)	voxel size	1.5 mm
	signal model	water-fat
	regularization parameter $\lambda$	$10^0$
	sampling neighborhood (ppm)	[-2.5, 2.5]
3 Low-res (WFS)	voxel size	3 mm
	signal model	water-fat-silicone
	regularization parameter $\lambda$	$10^{-4}$
	sampling neighborhood (ppm)	[-0.4, 0.4 + $\Delta_{WF}$ ]
4 Mid-res (WFS)	condition	if silicone is present
	voxel size	1.5 mm
	signal model	water-fat-silicone
	regularization parameter $\lambda$	$10^{-4}$
5 High-res	condition	if silicone is present (or if silicone is not present)
	voxel size	recon. voxel size
	signal model	water-fat-silicone (or water-fat)
	regularization parameter $\lambda$	$10^0$
6 Refinement	condition	only for regions with PDSF < 10%
	voxel size	recon. voxel size
	signal model	water-fat
	regularization parameter $\lambda$	$10^0$
6 Refinement	sampling neighborhood (ppm)	[-0.4, 0.4]
	insertion neighborhood (ppm)	[-0.4, 0.4]

If  $\frac{N_C}{N_{\text{total}}} > 0.01$ , silicone is detected.  $N_{\text{total}}$  is the total number of voxels and  $N_C$  is the number of elements in the set  $C$  with  $C$  being the largest set of connected voxel with PDSF > 0.6. Otherwise, water-fat separation with an additional *High-res* (WF) graph-cut layer is performed. The presence of silicone implants can also be prior information.

If silicone is present, the resolution of the water-fat-silicone field-map is increased in the *Mid-res* (WFS) and *High-res* (WFS) layer. The solution of the water-fat and low resolution water-fat-silicone separation is added as graph nodes to account for noise-dominated voxels.

To improve the field-map in tissue, a voxel-dependent signal model is applied in the last *Refinement* graph-cut layer. If PDSF < 0.1, it is assumed that no silicone is present in these voxels and, thus, the water-fat signal model is assumed (Fig. 4).

Based on the global optimal field-map yielded by the layered graph-cuts, the images are calculated. Proton density fat fraction (PDFF) maps are calculated with correction for  $R_2^*$  using the generalized proton density fraction PDFF =  $\eta_F$ . If no silicone implants are present, the water-fat signal model is assumed for the image and  $R_2^*$  calculation. Otherwise,

TABLE II

MR SCAN PARAMETERS FOR THE PHANTOM AND IN VIVO MEASUREMENTS. A MONOPLANAR TIME-INTERLEAVED MULTI-ECHO GRADIENT ECHO SEQUENCE [25] WAS USED

Parameter	Phantom measurement (2 scans with different echo times)	Breast dataset (20 subjects: 10 without silicone implant, 5 with a unilateral silicone implant and 5 with bilateral silicone implants)
TE	$N_{TE} = 6$ , $TE_1 = 1.24$ ms, $\Delta TE = 0.99$ ms; $N_{TE} = 6$ , $TE_1 = 1.58$ ms, $\Delta TE = 1.28$ ms	$N_{TE} = 6$ , $TE_1 = 1.58$ ms, $\Delta TE = 1.28$ ms
TR	8.08 ms; 9.62 ms	12.21 ms
flip angle	3°	3°
scan time	3:34 min; 4:23 min	4:15 min
FOV	187x220x190.5 mm <sup>3</sup>	220x382.6x192.4 mm <sup>3</sup>
voxel size (acquisition)	1.5 mm (isotropic)	1.3 mm (isotropic)
field strength	3 T (Philips Elition, Philips Healthcare, Best, The Netherlands)	3 T (Philips Ingenia, Philips Healthcare, Best, The Netherlands)
acceleration	-	SENSE + compressed sensing (R = 6)
reconstruction	online	custom reconstruction with BART [39]

the voxel-dependent signal model is assumed based on the threshold PDSF < 0.1.

### C. Implementation Details

The sampling step size for field-mapping is set to 2 Hz and the sampling range for the first graph-cut layer is set to  $\alpha_f * [-f_{B,\text{period}}/2, f_{B,\text{period}}/2]$  ( $\alpha_f = 2$  for the phantom study,  $\alpha_f = 2.5$  for the in vivo study). For  $R_2^*$ , the global minimum is searched voxel-wise in a sampling interval [0, 500] Hz with a sampling step size of 2 Hz. For phantom measurements, a threshold  $T = 2.5\%$  is applied for the mask  $M$ . A threshold  $T = 7.5\%$  is used for in vivo measurements. The value for  $T$  was chosen empirically based on the scan's noise performance to ensure connected voxels in the low-resolution graph-cut layers.

The proposed framework was implemented in Python. The graph-cut algorithm itself is intrinsically limited to a single CPU core and uses the PyMaxflow<sup>1</sup> library for graph construction and solving. The source code, including phantom data and examples used for this study, will be made publicly available: <https://github.com/BMRRgroup/fieldmapping-hmrGC>

## IV. EXPERIMENTS AND RESULTS

### A. MR Measurements

Phantom and in vivo measurements were performed to test the method and show the generalizability. MR scan parameters are summarized in Table II. Either all 6 echoes or the first 4 echoes were used for water-fat-silicone separation.

<sup>1</sup><https://github.com/pmneila/PyMaxflow>

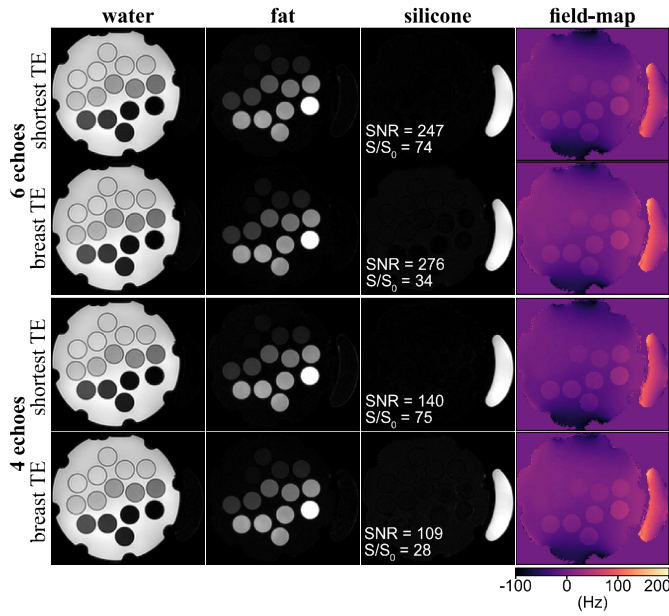


**Fig. 5.** Water-fat-silicone separation in the phantom for different echo times and number of echoes. The phantom was composed of water-fat vials inserted in water and a silicone implant.  $\Delta TE = 1.28$  ms was the echo spacing for breast imaging with the applied gradient echo sequence (Table II).  $\Delta TE = 0.99$  ms corresponded to the shortest echo times for the phantom scan. The SNR and the water-fat suppression performance ( $S/S_0$ ) were evaluated for the silicone images.

**1) Phantom Measurements:** A commercially available water-fat phantom (Calimatrix, Madison, WI, United States) and a silicone implant, placed next to each other, were scanned with different echo times using a monopolar time-interleaved multi-echo gradient echo sequence [25] (Table II). Each scan was acquired twice for a subsequent SNR calculation based on the difference image. A peanut oil fat model accounting for the temperature shift of the water peak was assumed for post-processing [40]. The phantom enclosed vials with a different fat fraction ranging between 0 and 100%, immersed in a water bath. Magnetic resonance spectroscopy (MRS) was performed for all vials to estimate a reference fat fraction (Stimulated Echo Acquisition Mode (STEAM), echo time  $TE = [10, 15, 20, 25, 75]$  ms, repetition time  $TR = 5000$  ms, mixing time  $TM = 17$  ms, voxel size =  $[10, 10, 30]$  mm, NSA = 4). Peak fitting was performed using a custom MRS toolbox (10-peak fat model and single water peak) [41].

**2) In Vivo Breast Measurements:** Clinical routine MR image data of the breast in 20 patients were retrospectively analyzed. The in vivo study part was approved by the local institutional review board (Klinikum rechts der Isar, Technical University of Munich, Munich, Germany). The present in vivo dataset contained MR scans of 20 women using the aforementioned gradient echo sequence. 10 subjects had silicone implants with 5 subjects with bilateral silicone implants and 5 subjects with a unilateral silicone implant (Table II). Method hyperparameters were adjusted based on a validation dataset with similar scan parameters. An in vivo bone marrow fat model was assumed for post-processing [42], [43]. Additionally, the dataset contained silicone-only scans with a water- and fat-suppressed sequence, which is used clinically at our institution to assess

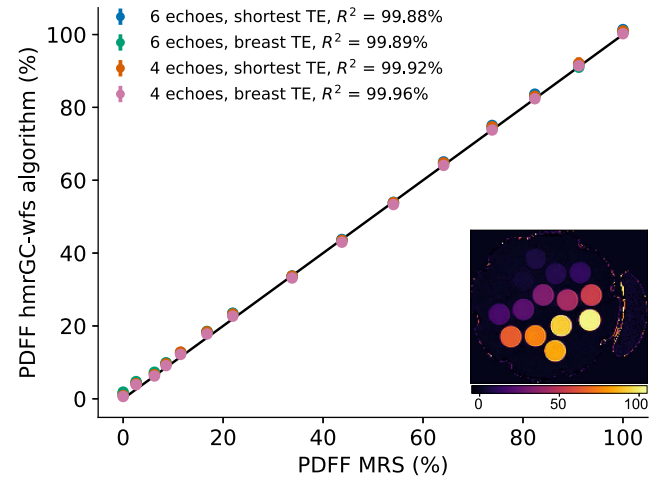


**Fig. 6.** Mean proton density fat-fraction (PDFFF) for different water-fat compositions. Chemical shift encoding-based gradient echo imaging using the hmrGC-wfs separation algorithm (y-axis) was compared with magnetic resonance spectroscopy (MRS, x-axis). The black line is the identity line. An exemplary PDFFF map of the phantom is shown in the bottom right corner.

implant integrity (T2-weighted turbo spin echo DIR acquisition,  $TE = 65$  ms, inversion time  $TI1/TI2 = 3100/220$  ms,  $TR = 15.7$  s, scan time = 3:08 min, field of view  $FOV = 220 \times 388.2 \times 187.8$  mm<sup>3</sup>, acquisition voxel size =  $[1.25, 1.88, 3]$  mm, C-SENSE with  $R = 3.5$ ).

## B. Evaluation Metrics

The performance of the proposed method was tested by comparing computational speed, the number of field-map swaps and the noise and suppression performance with the vlGC algorithm [18] and different echo times. Results were compared additionally to MRS and a conventional silicone-only scan. For water-fat-silicone separation, the vlGC algorithm was modified for the water-fat-silicone signal model (vlGC-wfs) [22]. The vlGC-wfs algorithm also applies a data cost term in its energy function with  $\lambda = 10^{-4}$ .

To count chemical species swaps, the field-map, water, fat and eventually silicone images were visually evaluated side by side for every slice and swaps were determined by rapid changes in the field-map and an abnormal water, fat or silicone distribution.

SNR was calculated based on two acquisitions with similar scan parameters (intensities  $I_1$  and  $I_2$  in a region of interest (ROI)) [44]:

$$SNR = \frac{1}{\sqrt{2}} \frac{\text{mean}_{\mathbf{r} \in \text{ROI}} (I_1(\mathbf{r}) + I_2(\mathbf{r}))}{\text{stddev}_{\mathbf{r} \in \text{ROI}} (I_1(\mathbf{r}) - I_2(\mathbf{r}))} \quad (15)$$

The water and fat suppression was quantified using the ratio between the mean signal intensity in the silicone implant  $S$  and a water-fat-only region  $S_0$ :

$$S/S_0 = \frac{\text{mean}_{\mathbf{r} \in \text{ROI}_S} I(\mathbf{r})}{\text{mean}_{\mathbf{r} \in \text{ROI}_{WF}} I(\mathbf{r})} \quad (16)$$

For the phantom, a ROI in the center of the silicone implant ( $41.3 \times 13.8$  mm<sup>2</sup>) was selected for the SNR and PDSF evaluation. Another ROI in the center of the water-fat phantom

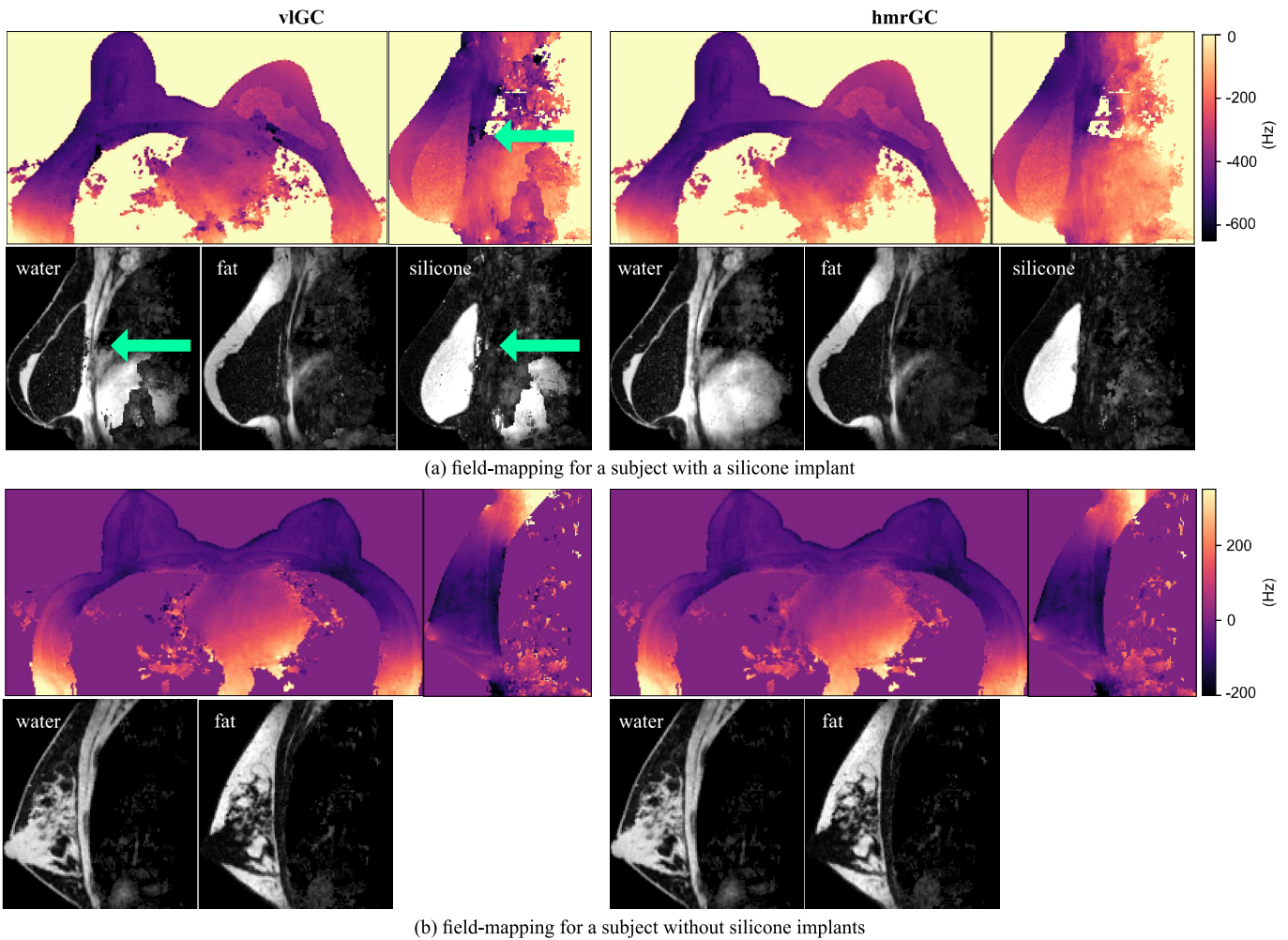


**Fig. 7.** Field-mapping results for the hierarchical multi-resolution method (hmrGC-wfs) and the variable-layer single-min-cut graph-cut methods (vIGC, vIGC-wfs). Axial and sagittal slices for the field-map and sagittal water, fat (and silicone) images are shown for two subjects (**a**: with silicone, **b**: without silicone). Arrows indicate water-silicone swaps.

( $41.3 \times 41.3 \text{ mm}^2$ ) was chosen for computing the  $S/S_0$  ratio. PDFF quantification in the phantom was evaluated by defining central ROIs of size  $13.8 \times 13.8 \times 27.5 \text{ mm}^3$  for each water-fat vial.

For the in vivo breast measurements, different ROIs (approx.  $16.5 \times 16.5 \text{ mm}^2$ ) were placed in breast tissue and the silicone implant to quantify the water-fat suppression ( $S/S_0$  ratio) in the separated silicone images and in the magnitude images of the conventional silicone-only scan.

### C. Phantom Results

Figure 5 shows water, fat and silicone images and the field-map in the phantom for different sequence parameters. The echo times  $TE_1/\Delta TE$  and the number of acquired echoes  $N_{TE}$  were varied. Robust water-fat-silicone separation is shown for each combination. A reduced noise performances can be observed for 4 echoes. The mean PDSF and standard deviation were evaluated in the silicone implant: 6 echoes,  $\Delta TE = 0.99 \text{ ms}$ : ( $102.6 \pm 1.0$ )%; 6 echoes,  $\Delta TE = 1.28 \text{ ms}$ : ( $99.9 \pm 1.4$ )%; 4 echoes,  $\Delta TE = 0.99 \text{ ms}$ : ( $98.9 \pm 1.9$ )%; 4 echoes,  $\Delta TE = 1.28 \text{ ms}$ : ( $97.7 \pm 1.8$ )%. The measured SNR

was in agreement with the theoretical CRLB analysis. The silicone images showed an improved water-fat suppression for the shortest possible echo times ( $\Delta TE = 0.99 \text{ ms}$ ).

The mean PDFF for different water-fat compositions was compared with MRS in Fig. 6. A good agreement between the separation-based PDFF using the hmrGC-wfs algorithm and the reference was found ( $R^2 > 99.8\%$ ). Only small differences were found for different applied sequence parameters.

### D. In Vivo Results

The hierarchical multi-resolution method performed robust separation in the breast without water-fat-silicone swaps for all 20 subjects. For some subjects, swaps occurred in noise- and motion-dominated regions outside of the breast and at the edge of the FOV.

Figure 7 compares the field-map for the hierarchical multi-resolution method and the vIGC and vIGC-wfs algorithm. The subject with silicone implants showed water-silicone swaps when the vIGC-wfs algorithm was used. Water-silicone swaps occurred especially in motion-affected regions (i.e. the heart) or at the implant's border. For the subject without silicone

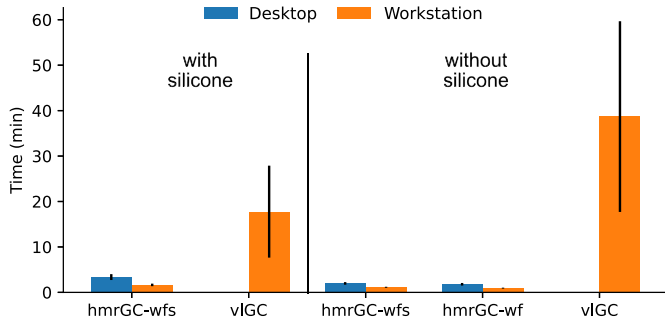


**Fig. 8.** Computational speed for the hierarchical multi-resolution methods (hmrGC-wfs, hmrGC-wf) and the variable-layer single-min-cut graph-cut methods (vIGC, vIGC-wfs). Subjects with and without implants were evaluated separately for 4 echoes and mean values and standard deviations are shown.

implants, similar field-maps, except for regions dominated by noise, were reported. Separated images had a similar noise performance for the hmrGC-wfs and the vIGC-wfs methods.

The computational speed comparison in Fig. 8 shows a significant decrease in computational time for the hmrGC methods compared to the vIGC and vIGC-wfs methods. The computational time was increased for the hmrGC-wfs method compared to the hmrGC-wf method. In the processing of the 6 echoes data, the hmrGC methods took similar time but processing time was significantly increased for the vIGC/vIGC-wfs methods (multiple hours). Lower memory constraints for the hmrGC methods also allowed the execution on machines with limited RAM (< 32 GB).

Sagittal and axial water, fat and silicone images and the field-map are shown in Fig. 9 for 6 and 4 echoes. Images showed a good agreement for the different number of echoes and no water-fat-silicone swaps. The region corresponding to the silicone implant in the 4-echo water and fat images and the field-map look noisier compared to the 6-echo acquisition. This is consistent with the lower noise performance observed in the phantom (Fig. 5) for 4 echoes. The water-fat suppression was slightly improved in the silicone image based on 6 echoes ( $S/S_0 = 32$  vs.  $S/S_0 = 26$ ).

Figure 10 presents three subjects with silicone implants and compares the clinically used silicone-only scan with the silicone image based on the proposed hmrGC-wfs method using the 4-echo gradient echo data. Additionally, the PDSF is shown as an additional contrast which can be used in the quantitative assessment of silicone per voxel. Especially in the sagittal slice, the separated silicone images had a significantly higher resolution. The clinically used silicone-only images exhibited higher signal in non-silicone regions (most notably in fat-dominated regions,  $(S/S_0)_{\text{hmrGC-wfs}} > 3 \cdot (S/S_0)_{\text{silicone-only}}$ ) and appeared more blurry compared to the silicone-separated images.

In Fig. 11, the fitted  $R_2^*$  maps used for PDSF and PDFF calculation are shown. The  $R_2^*$ -fit was considerably improved for 6 echoes compared to 4 echoes.

Figure 12 shows PDFF maps for 4 and 6 echoes and the water-fat and water-fat-silicone model. For the comparison of 4 and 6 echoes, quantification errors of up to 5% can

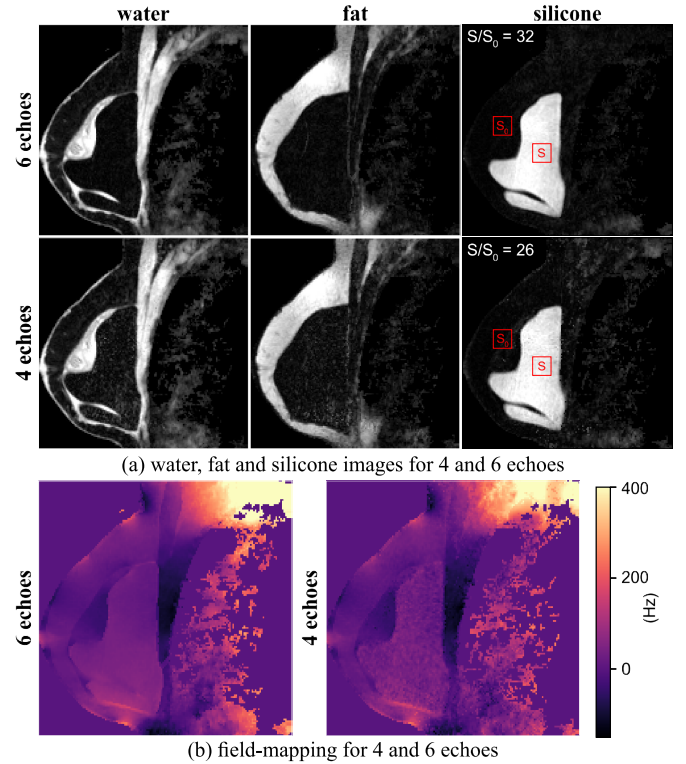


**Fig. 9.** In vivo water-fat-silicone separation results for a subject with silicone implants. Water, fat and silicone images (a) and the field-map (b) are shown for a sagittal slice for 4 and 6 echoes. Water-fat suppression in the silicone image was quantified using the  $S/S_0$  ratio. The ROIs are highlighted in red.

be estimated in the breast. Furthermore, PDFF quantification was compared using the water-fat-silicone or water-fat signal model for 4 echoes. The comparison showed concordant results with small deviations of up to 1% per voxel. Outside of the breast, higher quantification errors were estimated.

## V. DISCUSSION

A framework for field-mapping in CSE-MRI was developed in the present work. In particular, a novel algorithm was introduced for the joint estimation of water, fat and silicone images in in vivo breast CSE-MRI. Robustness and competitive processing times were achieved by performing graph-cuts using varying spatial resolutions. The hierarchical use of signal models and the linkage of graph-cut layers assured a high accuracy and SNR.

The proposed method enables improved water-fat suppression, less blurring and isotropic resolution compared to the clinically used silicone-only scans employed in the routine imaging protocol in our institution. The examination time may be significantly reduced since only a single sequence is necessary for obtaining water, fat and silicone images, especially when PDFF quantification (e.g. quantifying breast density) or quantitative susceptibility mapping (e.g. detecting breast calcifications [45], [46]) are of interest. The proposed method may be useful in detecting silicone implant's ruptures. The improved image quality may enable the detection of rare complications, i.e. silicone-induced lymphadenopathy. Ruptures or

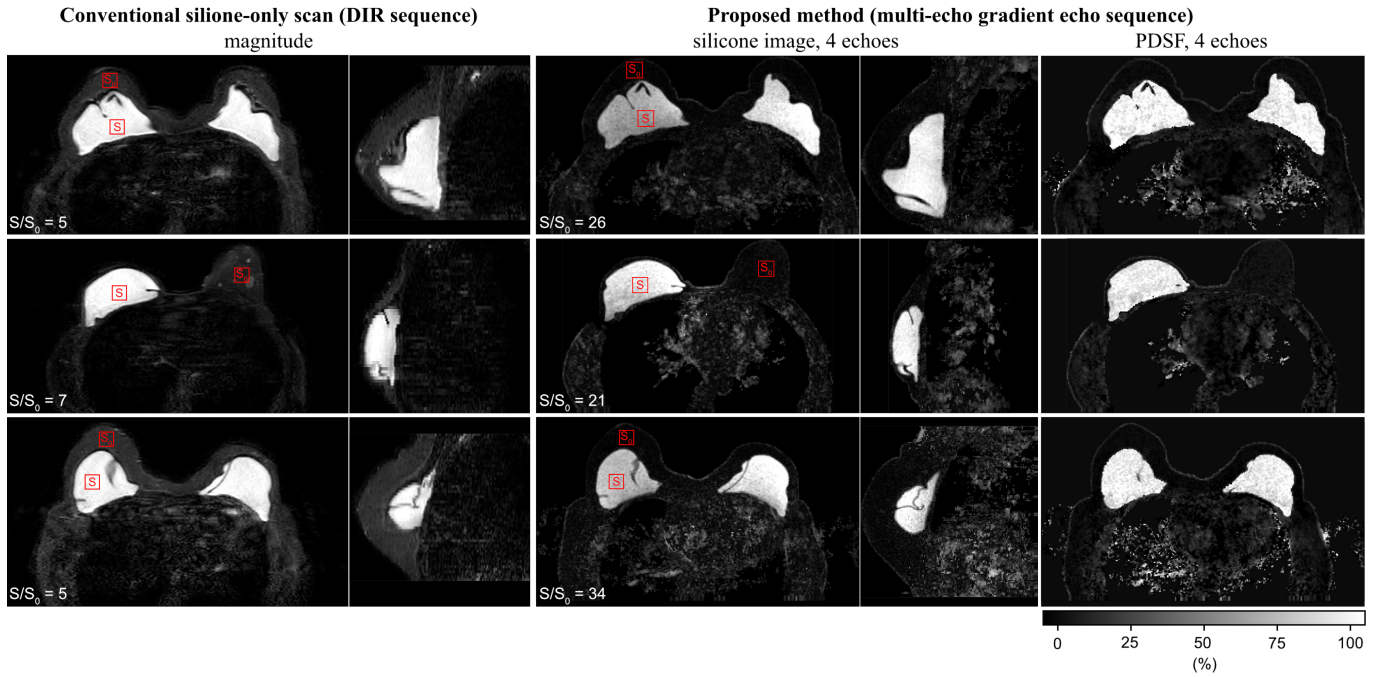


**Fig. 10.** Clinically used silicone-only scan (double inversion recovery (DIR) acquisition) compared with water-fat-silicone separation based on 4 echoes (multi-echo gradient echo acquisition). Axial and sagittal slices are depicted for the silicone-only scan, the separated silicone images and the separation-based proton density silicone-fraction (PDSF). Water-fat suppression in the silicone-only scans and the separated silicone images was quantified using the  $S/S_0$  ratio. The ROIs are highlighted in red.

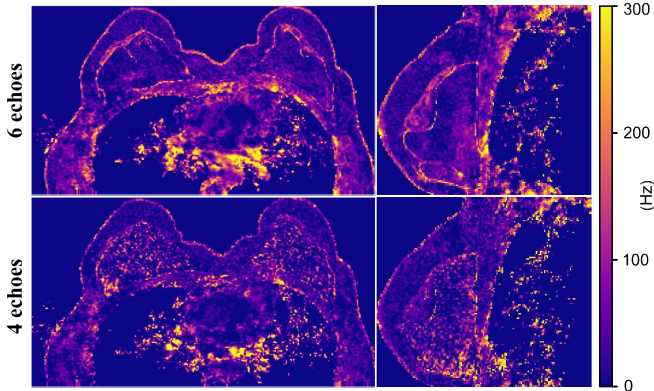


**Fig. 11.**  $F_2^*$  maps for a subject with a silicone implant. Axial and sagittal slices for 4 and 6 echoes are shown.

gel bleeding can lead to silicone leakage accumulating in lymph nodes, which can be challenging to diagnose based on conventional MR imaging due to overlying pulsation artifacts of thoracic organs [47], [48].

The proposed use of different spatial resolutions decreases processing times ( $< 5$  min) and enables water-fat(-silicone) separation with a reduced number of echoes even in the presence of low SNR. It was shown that the proposed method can reduce water-fat-silicone swaps for 4 echoes compared to a single-resolution modified vIGC implementation (vIGC-wfs method). Four echoes are the minimum number of echoes needed for water-fat-silicone separation, but the noise performance is reduced additionally due to non-optimal in vivo echo times constrained by the in vivo voxel size. In the proposed

method, the solution for voxels with unreliable minima estimation is estimated using the downsampled signal (Fig. 3). Similar improvements were shown by other multi-resolution water-fat separation methods [11]–[14]. However, other multi-resolution methods did not yield an unwrapped field-map and, although the field-map is first computed using a downsampled signal, a non-smoothed field-map is estimated with the same accuracy as for the vIGC method. In further studies, the application of the algorithm for water-fat separation in other anatomies could show its benefit to handle disjoint regions. Graph-cut layers with a low spatial resolution may be used to map a field-map estimate for signal voids based on the local minima of neighboring voxels.

The hierarchical decomposition of the separation problem consists of layered graph-cuts with different signal models, sampling ranges and regularization. The first graph-cut layers are computed with the water-fat signal model for higher robustness and computational speed. The number of local minima of the residual error is increasing with the number of chemical species in the signal model (Fig. 2) and, thus, the number of graph nodes is decreased if a water-fat model instead of a water-fat-silicone model is applied. The worst-case complexity of the applied Boykov-Kolmogorov algorithm is increasing quadratically with the number of graph nodes [35]. For some geometries, if the fraction of signal voxels with silicone is large (e.g., phantom measurements with only a silicone implant), assuming a water-fat-silicone model in the unwrapping layer might be more appropriate. Furthermore, the use of different signal models per voxel is allowed in the proposed method. The refinement of the field-map for voxels without silicone, i.e. voxels with tissue, increases the accuracy

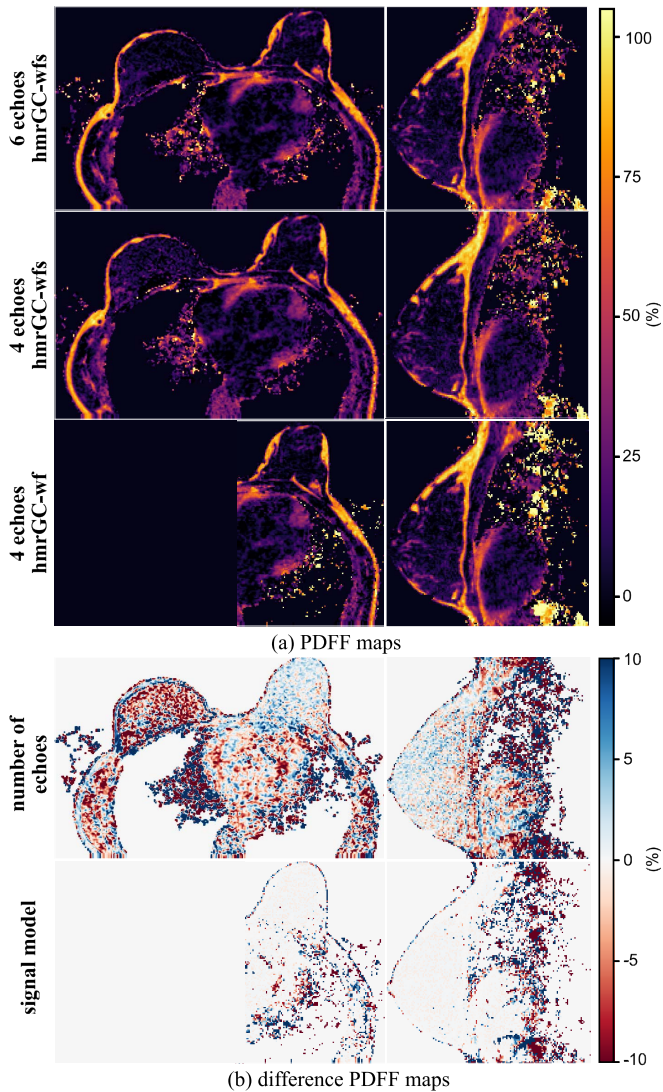


**Fig. 12.** Proton density fat-fraction (PDFF) maps (a) for water-fat-silicone separation (hmrGC-wfs) based on 4 or 6 echoes and water-fat separation (hmrGC-wf) based on 4 echoes. The dataset was cropped to only include the breast without implant for water-fat separation. Difference PDFF maps (b) are shown for the number of echoes ( $\text{PDFF}_{\text{wfs},6 \text{ echoes}} - \text{PDFF}_{\text{wfs},4 \text{ echoes}}$ ), and the signal model ( $\text{PDFF}_{\text{wfs},4 \text{ echoes}} - \text{PDFF}_{\text{wf},4 \text{ echoes}}$ ).

of the method. Results for the hmrGC-wfs method showed similar PDFF values compared to the hmrGC-wf method in a breast without silicone implant.

Each of the graph-cut layers applies a modified vGC algorithm due to favorable properties: it converges to the global minimum of the energy function [34] and the algorithm is able to resolve large field-map variations [18]. The energy function was modified for an additional data-consistency term weighted by the inverse of a regularization parameter. However, further optimization of the energy function might improve the performance of the algorithm.

The presented method could be similarly applied for water-fat-silicone imaging at 1.5 T. The graph-cut algorithm normalizes the field-map distance on the static magnetic field strength and thus is independent of the field strength. The resonance

frequencies of fat and silicone are closer to the water resonance frequency at 1.5 T but a similar performance compared to 3 T could be expected if longer and appropriate echo times corresponding to the same phase differences for the chemical species are applied. The experimental design can be simplified for longer optimal echo times and a monopolar sequence could be applied without time-interleaving.

The presented method was adjusted for three or more echoes (four or more echoes for water-fat-silicone separation) but the framework could be adapted for water-fat separation with only two acquired echoes [49] or phase unwrapping. Additionally, the framework might be useful for three chemical species separation in the body other than water-fat-silicone separation, i.e.  $^{13}\text{C}$  metabolic imaging [50].

Previous works have attempted to separate silicone from the water-fat signal using CSE-MRI. Selective imaging of silicone was proposed by separating all three species while setting the center frequency on the silicone peak and assuming zero field-map variations [51]. Furthermore, a 3D water-silicone separation combined with STIR for fat suppression was presented allowing to increase the spatial resolution [4], but with the known limitations of STIR in reducing SNR and lengthening scan time [52]. Related works on the simultaneous separation of water, fat and silicone [12], [21] were only performed in a simplified phantom. Moreover, the approaches were limited due to the needed initialization with a field-map [21] or the direct phase estimation [12].

The present work has some limitations. First, although computational time was significantly reduced, the graph-cut algorithm itself is intrinsically not parallelizable without a loss of accuracy [53]–[55]. Further optimization can exchange some graph-cut layers with neural networks or optimize the number of multi-resolution graph-cut layers. Second, the method was only tested for a field strength of 3 T and for sequences with constant echo spacing. Although the multi-resolution framework can be easily adapted for non-equidistant echoes, the hierarchical decomposition of the water-fat-silicone separation relies on the periodicity of the residual  $C(f_B)$  for estimating sampling neighborhoods. Third, the hierarchical multi-resolution framework was only applied for breast MRI. However, fast and accurate field-mapping has a larger field of application in the body (e.g. liver [56], [57], spine [18], [20]). Fourth, the performance of the algorithm can be limited by noise-dominated or corrupted regions where the signal is unreliable. Although the optimization is improved due to the multi-resolution approach, signal masking has a high importance. The chosen threshold  $T$  was chosen to perform separation automatically for all 10 subjects, but a subject-specific threshold might be beneficial to minimize swaps in the noise-dominated and motion-corrupted regions at the edge of the FOV.

## VI. CONCLUSION

A hierarchical multi-resolution graph-cut framework was developed and proposed for water-fat and water-fat-silicone separation. The proposed method enables *in vivo* simultaneous water-fat-silicone separation and shows robust separation also

for limited and noisy data. The presented algorithm also enables PDFF quantification and field-mapping in subjects with silicone implants with the same accuracy as for water-fat separation. The derived silicone-separated images have the ability to overcome limitations of clinically used silicone-only scans in terms of water-fat suppression, image blurring and spatial resolution.

### ACKNOWLEDGMENT

The authors would like to thank Dr. Christoph Heitmann, Seno-MVZ, Munich, Germany, for providing different silicone implant types for ex vivo scanning.

### REFERENCES

- [1] S. L. Brown, B. G. Silverman, and W. A. Berg, "Rupture of silicone-gel breast implants: Causes, sequelae, and diagnosis," *Lancet*, vol. 350, no. 9090, pp. 1531–1537, Nov. 1997.
- [2] S. Mukundan, W. D. Thomas, B. D. Kruse, D. L. Monticciolo, and R. C. Nelson, "MR imaging of silicone gel-filled breast implants *in vivo* with a method that visualizes silicone selectively," *J. Magn. Reson. Imag.*, vol. 3, no. 5, pp. 713–717, Sep. 1993.
- [3] D. L. Monticciolo, R. C. Nelson, W. T. Dixon, J. Bostwick, S. Mukundan, and T. R. Hester, "MR detection of leakage from silicone breast implants: Value of a silicone-selective pulse sequence," *Amer. J. Roentgenol.*, vol. 163, no. 1, pp. 51–56, Jul. 1994.
- [4] A. J. Madhuranthakam *et al.*, "Water-silicone separated volumetric MR acquisition for rapid assessment of breast implants," *J. Magn. Reson. Imag.*, vol. 35, no. 5, pp. 1216–1221, Jan. 2012.
- [5] J. Ding *et al.*, "Reproducible automated breast density measure with, no., ionizing radiation using fat-water decomposition MRI," *J. Magn. Reson. Imag.*, vol. 48, no. 4, pp. 971–981, Apr. 2018.
- [6] S. B. Reeder, H. H. Hu, and C. B. Sirlin, "Proton density fat-fraction: A standardized mr-based biomarker of tissue fat concentration," *J. Magn. Reson. Imag.*, vol. 36, no. 5, pp. 1011–1014, Jul. 2012.
- [7] L. C. H. Bancroft *et al.*, "Proton density water fraction as a reproducible MR-based measurement of breast density," *Magn. Reson. Med.*, vol. 87, no. 4, pp. 1742–1757, Nov. 2021.
- [8] N. F. Boyd *et al.*, "Mammographic density and the risk and detection of breast cancer," *New England J. Med.*, vol. 356, no. 3, pp. 227–236, 2007.
- [9] H. Yu, S. B. Reeder, A. Shimakawa, J. H. Brittain, and N. J. Pelc, "Field map estimation with a region growing scheme for iterative 3-point water-fat decomposition," *Magn. Reson. Med.*, vol. 54, no. 4, pp. 1032–1039, Oct. 2005.
- [10] J. Berglund, L. Johansson, H. Ahlström, and J. Kullberg, "Three-point Dixon method enables whole-body water and fat imaging of obese subjects," *Magn. Reson. Med.*, vol. 63, no. 6, pp. 1659–1668, 2010.
- [11] W. Lu and B. A. Hargreaves, "Multiresolution field map estimation using golden section search for water-fat separation," *Magn. Reson. Med.*, vol. 60, no. 1, pp. 236–244, Jul. 2008.
- [12] J. Tsao and Y. Jiang, "Hierarchical IDEAL: Fast, robust, and multiresolution separation of multiple chemical species from multiple echo times," *Magn. Reson. Med.*, vol. 70, no. 1, pp. 155–159, Aug. 2012.
- [13] J. Berglund and M. Skorpil, "Multi-scale graph-cut algorithm for efficient water-fat separation," *Magn. Reson. Med.*, vol. 78, no. 3, pp. 941–949, Oct. 2016.
- [14] J. Andersson, H. Ahlström, and J. Kullberg, "Water-fat separation incorporating spatial smoothing is robust to noise," *Magn. Reson. Imag.*, vol. 50, pp. 78–83, Jul. 2018.
- [15] D. Hernando, P. Kellman, J. P. Haldar, and Z.-P. Liang, "Robust water/fat separation in the presence of large field inhomogeneities using a graph cut algorithm," *Magn. Reson. Med.*, vol. 63, no. 1, pp. 79–90, Jan. 2010.
- [16] C. Cui, X. Wu, J. D. Newell, and M. Jacob, "Fat water decomposition using globally optimal surface estimation (GOOSE) algorithm," *Magn. Reson. Med.*, vol. 73, no. 3, pp. 1289–1299, Mar. 2014.
- [17] C. Cui, A. Shah, X. Wu, and M. Jacob, "A rapid 3D fat-water decomposition method using globally optimal surface estimation (R-GOOSE)," *Magn. Reson. Med.*, vol. 79, no. 4, pp. 2401–2407, Jul. 2017.
- [18] C. Boehm, M. N. Diefenbach, M. R. Makowski, and D. C. Karampinos, "Improved body quantitative susceptibility mapping by using a variable-layer single-min-cut graph-cut for field-mapping," *Magn. Reson. Med.*, vol. 85, no. 3, pp. 1697–1712, Nov. 2020.
- [19] R. Jafari *et al.*, "Deep neural network for water/fat separation: Supervised training, unsupervised training, and no training," *Magn. Reson. Med.*, vol. 85, no. 4, pp. 2263–2277, Oct. 2020.
- [20] C. Boehm *et al.*, "Preconditioned water-fat total field inversion: Application to spine quantitative susceptibility mapping," *Magn. Reson. Med.*, vol. 87, no. 1, pp. 417–430, Jan. 2022.
- [21] S. B. Reeder *et al.*, "Multicoil Dixon chemical species separation with an iterative least-squares estimation method," *Magn. Reson. Med.*, vol. 51, no. 1, pp. 35–45, 2003.
- [22] J. K. Stelter *et al.*, "Optimal experimental design for quantitative water, fat and silicone separation using a variable projection method with 4 or 6 echoes at 3T," in *Proc. ISMRM*, to be published.
- [23] M. Bydder *et al.*, "Relaxation effects in the quantification of fat using gradient echo imaging," *Magn. Reson. Imag.*, vol. 26, no. 3, pp. 347–359, Apr. 2008.
- [24] H. Yu *et al.*, "Phase and amplitude correction for multi-echo water-fat separation with bipolar acquisitions," *J. Magn. Reson. Imag.*, vol. 31, no. 5, pp. 1264–1271, May 2010.
- [25] S. Ruschke *et al.*, "Correction of phase errors in quantitative water-fat imaging using a monopolar time-interleaved multi-echo gradient echo sequence," *Magn. Reson. Med.*, vol. 78, no. 3, pp. 984–996, Oct. 2016.
- [26] G. H. Glover and E. Schneider, "Three-point Dixon technique for true water/fat decomposition with B0 inhomogeneity correction," *Magn. Reson. Med.*, vol. 18, no. 2, pp. 371–383, Apr. 1991.
- [27] S. B. Reeder *et al.*, "Iterative decomposition of water and fat with echo asymmetry and least-squares estimation (IDEAL): Application with fast spin-echo imaging," *Magn. Reson. Med.*, vol. 54, no. 3, pp. 636–644, 2005.
- [28] H. Yu, A. Shimakawa, C. A. McKenzie, E. Brodsky, J. H. Brittain, and S. B. Reeder, "Multiecho water-fat separation and simultaneous R2\* estimation with multifrequency fat spectrum modeling," *Magn. Reson. Med.*, vol. 60, no. 5, pp. 1122–1134, Nov. 2008.
- [29] D. P. Gorchyca *et al.*, "Silicone breast implant rupture: Comparison between three-point Dixon and fast spin-echo MR imaging," *Amer. J. Roentgenol.*, vol. 162, no. 2, pp. 305–310, Feb. 1994.
- [30] M. N. Diefenbach, C. Liu, and D. C. Karampinos, "Generalized parameter estimation in multi-echo gradient-echo-based chemical species separation," *Quant. Imag. Med. Surg.*, vol. 10, no. 3, pp. 554–567, Mar. 2020.
- [31] A. R. Pineda, S. B. Reeder, Z. Wen, and N. J. Pelc, "Cramér–Rao bounds for three-point decomposition of water and fat," *Magn. Reson. Med.*, vol. 54, no. 3, pp. 625–635, Sep. 2005.
- [32] D. Hernando, Z.-P. Liang, and P. Kellman, "Chemical shift-based water/fat separation: A comparison of signal models," *Magn. Reson. Med.*, vol. 64, no. 3, pp. 811–822, Jun. 2010.
- [33] D. Hernando, J. P. Haldar, B. P. Sutton, J. Ma, P. Kellman, and Z.-P. Liang, "Joint estimation of water/fat images and field inhomogeneity map," *Magn. Reson. Med.*, vol. 59, no. 3, pp. 571–580, Mar. 2008.
- [34] A. Shah, M. D. Abámoff, and X. Wu, "Optimal surface segmentation with convex priors in irregularly sampled space," *Med. Image Anal.*, vol. 54, pp. 63–75, May 2019.
- [35] Y. Boykov and V. Kolmogorov, "An experimental comparison of min-cut/max-flow algorithms for energy minimization in vision," *IEEE Trans. Pattern Anal. Mach. Intell.*, vol. 26, no. 9, pp. 1124–1137, Sep. 2004.
- [36] A. Telea, "An image inpainting technique based on the fast marching method," *J. Graph. Tools*, vol. 9, no. 1, pp. 23–34, 2004.
- [37] J. A. Sethian, "A fast marching level set method for monotonically advancing fronts," *Proc. Nat. Acad. Sci. USA*, vol. 93, no. 4, pp. 1591–1595, 1996.
- [38] C.-Y. Liu, C. A. McKenzie, H. Yu, J. H. Brittain, and S. B. Reeder, "Fat quantification with IDEAL gradient echo imaging: Correction of bias from T1 and noise," *Magn. Reson. Med.*, vol. 58, no. 2, pp. 354–364, Aug. 2007.
- [39] M. Uecker *et al.*, "Mrirecon/bart: Version 0.7.00," Tech. Rep., 2021. [Online]. Available: <https://github.com/mrirecon/bart/tree/v0.7.00>, doi: 10.5281/zenodo.4570601.
- [40] M. Bydder, O. Girard, and G. Hamilton, "Mapping the double bonds in triglycerides," *Magn. Reson. Imag.*, vol. 29, no. 8, pp. 1041–1046, Oct. 2011.
- [41] S. Ruschke and D. C. Karampinos, "ALFONSO: A versatile formulation for N-dimensional signal model fitting of MR spectroscopy data and its application in MRS of body lipids," in *Proc. ISMRM*, to be published.
- [42] J. Ren, I. Dimitrov, A. D. Sherry, and C. R. Malloy, "Composition of adipose tissue and marrow fat in humans by 1H NMR at 7 Tesla," *J. Lipid Res.*, vol. 49, no. 9, pp. 2055–2062, Sep. 2008.

- [43] G. Hamilton *et al.*, “*In vivo* triglyceride composition of abdominal adipose tissue measured by 1 h MRS at 3T,” *J. Magn. Reson. Imag.*, vol. 45, no. 5, pp. 1455–1463, May 2017.
- [44] O. Dietrich, J. G. Raya, S. B. Reeder, M. F. Reiser, and S. O. Schoenberg, “Measurement of signal-to-noise ratios in MR images: Influence of multichannel coils, parallel imaging, and reconstruction filters,” *J. Magn. Reson. Imag.*, vol. 26, no. 2, pp. 375–385, Aug. 2007.
- [45] A. Fatemi-Ardekani, C. Boylan, and M. D. Noseworthy, “Identification of breast calcification using magnetic resonance imaging,” *Med. Phys.*, vol. 36, no. 12, pp. 5429–5436, Nov. 2009.
- [46] F. Schweser *et al.*, “Quantitative magnetic susceptibility mapping (QSM) in breast disease reveals additional information for mr-based characterization of carcinoma and calcification,” in *Proc. ISMRM*, to be published.
- [47] P. R. Bauer, B. J. Krajcicek, C. E. Daniels, S. S. Shah, and J. H. Ryu, “Silicone breast implant-induced lymphadenopathy: 18 cases,” *Respiratory Med. CME*, vol. 4, no. 3, pp. 126–130, 2011.
- [48] Y. Lee, S. E. Song, E.-S. Yoon, J. W. Bae, and S. P. Jung, “Extensive silicone lymphadenopathy after breast implant insertion mimicking malignant lymphadenopathy,” *Ann. Surgical Treatment Res.*, vol. 93, no. 6, p. 331, 2017.
- [49] H. Eggers, B. Brendel, A. Duijndam, and G. Herigault, “Dual-echo Dixon imaging with flexible choice of echo times,” *Magn. Reson. Med.*, vol. 65, no. 1, pp. 96–107, Sep. 2010.
- [50] S. B. Reeder, J. H. Brittain, T. M. Grist, and Y.-F. Yen, “Least-squares chemical shift separation for  $^{13}\text{C}$  metabolic imaging,” *J. Magn. Reson. Imag.*, vol. 26, no. 4, pp. 1145–1152, Oct. 2007.
- [51] E. Schneider and T. W. Chan, “Selective MR imaging of silicone with the three-point Dixon technique,” *Radiology*, vol. 187, no. 1, pp. 89–93, Apr. 1993.
- [52] H. Eggers and P. Börnert, “Chemical shift encoding-based water-fat separation methods,” *J. Magn. Reson. Imag.*, vol. 40, no. 2, pp. 251–268, Jan. 2014.
- [53] V. Vineet and P. J. Narayanan, “CUDA cuts: Fast graph cuts on the GPU,” in *Proc. IEEE Comput. Soc. Conf. Comput. Vis. Pattern Recognit. Workshops*, Jun. 2008, pp. 1–8.
- [54] P. Strandmark and F. Kahl, “Parallel and distributed graph cuts by dual decomposition,” in *Proc. IEEE Comput. Soc. Conf. Comput. Vis. Pattern Recognit.*, Jun. 2010, pp. 2085–2092.
- [55] M. Yu, S. Shen, and Z. Hu, “Dynamic parallel and distributed graph cuts,” *IEEE Trans. Image Process.*, vol. 25, no. 12, pp. 5511–5525, Dec. 2016.
- [56] B. Guiu *et al.*, “Quantification of liver fat content: Comparison of triple-echo chemical shift gradient-echo imaging and *in vivo* proton MR spectroscopy,” *Radiology*, vol. 250, no. 1, pp. 95–102, Jan. 2009.
- [57] S. B. Reeder, I. Cruite, G. Hamilton, and C. B. Sirlin, “Quantitative assessment of liver fat with magnetic resonance imaging and spectroscopy,” *J. Magn. Reson. Imag.*, vol. 34, no. 4, pp. 729–749, Sep. 2011.